remote sensing

MDPI

Article

Evaluation of Fengyun-4B Satellite Temperature Profile Products Using Radiosonde Observations and ERA5 Reanalysis over Eastern Tibetan Plateau

Yuhao Wang [1,2], Xiaofei Wu [1], Haoxin Zhang [2], Hong-Li Ren [2,*] and Kaiqing Yang [1]

[1] Plateau Atmosphere and Environment Key Laboratory of Sichuan Province, School of Atmospheric Sciences, Chengdu University of Information Technology, Chengdu 610225, China; 3220101041@stu.cuit.edu.cn (Y.W.); wuxf@cuit.edu.cn (X.W.); yangkq@cuit.edu.cn (K.Y.)

[2] State Key Laboratory of Severe Weather, and Institute of Tibetan Plateau Meteorology, Chinese Academy of Meteorological Sciences, Beijing 100081, China; zhanghx@cma.gov.cn

* Correspondence: renhl@cma.gov.cn

Abstract: The latest-generation geostationary meteorological satellite, Fengyun-4B (FY-4B), equipped with the Geostationary Interferometric Infrared Sounder (GIIRS), offers high-spatiotemporal-resolution three-dimensional temperature structures. Its deployment serves as a critical complement to atmospheric temperature profile (ATP) observation in the Tibetan Plateau (TP). Based on radiosonde observation (RAOB) and the fifth-generation ECMWF global climate atmospheric reanalysis (ERA5), this study validates the availability and representativeness of FY-4B/GIIRS ATP products in the eastern TP region. Due to the issue of satellite zenith, this study focuses solely on examining the eastern TP region. Under a clear sky, FY-4B/GIIRS ATP exhibits good consistency with RAOB compared to cloudy conditions, with an average root mean square error (RMSE) of 2.57 K. FY-4B/GIIRS tends to underestimate temperatures in the lower layers while overestimating temperatures in the upper layers. The bias varies across seasons. Except for summer, the horizontal and vertical bias distribution patterns are similar, though there are slight differences in values. Despite the presence of bias, FY-4B/GIIRS ATP maintains a good consistency with observations and reanalysis data, indicating commendable product quality. These results demonstrate that it can play a vital role in augmenting the ATP observation network limited by sparse radiosonde stations in the eastern TP, offering crucial data support for numerical weather prediction, weather monitoring, and related meteorological research in this region.

Keywords: temperature profiles; Fengyun-4B; data validation; Tibetan Plateau

Citation: Wang, Y.; Wu, X.; Zhang, H.; Ren, H.-L.; Yang, K. Evaluation of Fengyun-4B Satellite Temperature Profile Products Using Radiosonde Observations and ERA5 Reanalysis over Eastern Tibetan Plateau. *Remote Sens.* **2024**, *16*, 4155. https://doi.org/10.3390/rs16224155

Academic Editor: Carmine Serio

Received: 27 September 2024
Revised: 5 November 2024
Accepted: 6 November 2024
Published: 7 November 2024

1. Introduction

As a key thermodynamic variable in the atmosphere, the atmospheric temperature profiles (ATPs) play a vital role in improving numerical simulation, climate prediction, and atmospheric monitoring [1–3]. Currently, radiosonde observations are the primary means of obtaining ATP data [4]. Tibetan Plateau (TP), the highest and most topographically complex plateau on the earth, is the source of several rivers and has been referred to as the world's third pole, affecting more than 20% of the global population [5]. More importantly, the eastern TP is home to one of the world's most critical biodiversity hotspots: the Hengduan Mountains Biodiversity Hotspot [6–8]. Additionally, over 90% of the TP's population resides in this region [9]. Enhancing the capability to observe meteorological elements in this area is crucial for protecting biodiversity and ensuring the safety of lives and property.

Nonetheless, in contrast to other land areas globally, there is a shortage of observational data over the Tibetan Plateau due to its high altitude, extreme environmental conditions, and underdeveloped logistical support. Although several field experiments

have been conducted in these data-deficient regions, including three Tibetan Plateau Atmospheric Scientific Experiments held in 1979, 1998, and from 2013 to 2021 [10–13], the observational data from these short-term experiments suffer from temporal and spatial resolution limitations. The intricate terrain and underlying surface characteristics further restrict the representativeness of the observation stations [14]. Therefore, high-resolution satellite remote sensing has the potential to effectively bridge the gap left by conventional observations in the eastern TP and its adjacent areas.

Satellite observation data have the advantages of wide coverage, and their high temporal and spatial resolution is less susceptible to the geographical environment [15,16], which makes up for the lack of sparse conventional observations over the TP area. Thus, it serves as an essential part of the meteorological observation network [17,18]. Among satellite-based observation instruments, the infrared detector greatly contributes to the research [19–21]. Hyperspectral infrared sounders (HIRs) feature thousands of channels with high spectral resolution, enabling precise measurement of the vertical profiles of atmospheric temperature and humidity [22].

The geostationary-satellite-based infrared hyperspectral sounder offers a higher scanning frequency compared to its polar orbit counterparts, which improves the applications of the ATP, especially in severe weather monitoring and predictions on the TP. In 2016 and 2021, China launched two second-generation geostationary meteorological satellites, Fengyun-4A (FY-4A) and Fengyun-4B (FY-4B), both equipped with the Geostationary Interferometric Infrared Sounder (GIIRS). The GIIRS became the first hyperspectral infrared sounder aboard a geostationary meteorological satellite [23]. It enabled high spatiotemporal resolution detection of weather systems in China and its surrounding regions, facilitating the acquisition of more detailed atmospheric vertical structures, including the retrieval of atmospheric temperature profiles at the 1 km layers [24] (http://fy4.nsmc.org.cn/nsmc/en/theme/FY4B.html, accessed on 5 November 2024). The development of the rapid radiative transfer model [25], the evaluation of bias characteristics [26], and advancements in retrieval algorithms [27–29] have facilitated the application of FY-4A/GIIRS data in numerical weather prediction models [30–32]. The atmospheric temperature and humidity profile products obtained from the onboard sounding instruments have significantly contributed to weather monitoring and forecasting [33,34].

The accuracy of satellite data is a crucial factor in ensuring the smooth progress of research and operations [35]. Before utilizing retrieval products, it is essential to assess the accuracy of the data and select appropriate data for use [2]. Scholars have conducted some research on FY-4A/GIIRS data quality evaluation. Yang et al. [24] conducted a comparative analysis between the temperature and humidity profiles retrieved from FY-4A/GIIRS and GOES using one-dimensional variational retrieval [36,37]; their study delineated that while the vertical root mean square error (RMSE) characteristics of the temperature and humidity profiles retrieved from FY-4A and GOES exhibit similarity, FY-4A/GIIRS demonstrates a lower RMSE compared to GOES. He et al. [38] and Du et al. [39] found that clouds would affect the quality of FY-4A/GIIRS ATP and different types and heights of clouds have different impacts on them. Some studies indicate that ATP from FY-4A/GIIRS can fill the observation gap caused by sparse conventional observations and have considerable value in assimilation applications [2,40,41].

Compared to FY-4A, the GIIRS on FY-4B features a broader spectral range, higher spectral resolution in the long-wave infrared band, and improved radiometric calibration accuracy and detection sensitivity [42]. Niu et al. [43] compared the quality of FY-4A/GIIRS and FY-4B/GIIRS long-wave infrared channels and pointed out that under clear sky conditions, the data error of FY-4B/GIIRS long-wave channels is smaller, and the daily variation in the error is also smaller. Benefiting from the increased spectral range, the ATP accuracy of FY-4B/GIIRS is higher than that of FY-4A/GIIRS and is more stable during the retrieving [42]. Yang et al. [44] used the fifth-generation European Centre for Medium-Range Weather Forecasts (ECMWF) atmospheric reanalysis (ERA5) data to evaluate the accuracy of FY-4B/GIIRS ATP, which showed that the FY-4B/GIIRS ATP has high overall accuracy, with

the RMSE values within 1K. Nevertheless, research about the ATP of FY-4B/GIIRS remains relatively scarce, especially over TP, due to the short timeframe of the product release.

The traditional method for validating satellite ATP involves the use of RAOB data [2,39,40]. The daily temporal resolution of RAOB data, which are available twice at 00 UTC and 12 UTC, is considered insufficient for a thorough evaluation and comparative analysis of the FY-4B/GIIRS ATP products over the Tibetan Plateau. This sparsity remains a major source of errors, and the cost and environmental impact of launching sufficient RAOBs to overcome this limitation hinder our ability to address the issue of data sparsity [45,46]. This issue motivates us to use ERA5 reanalysis data to test the performance of the FY-4B/GIIRS ATP products over TP. This study chose an entire year of ATP products from FY-4B/GIIRS to compare with RAOB, including nine routine sounding observations in the TP area from 17 January 2023 to 17 January 2024. Additionally, the ATP products were also compared with ERA5 reanalysis data, to compensate for RAOB's lack of temporal and spatial resolution.

The subsequent sections of this paper are structured as follows. Section 2 describes the dataset used in this study, as well as the matching strategy and some statistical criteria used for evaluation. In Sections 3–5, the bias characteristics of FY-4B/GIIRS ATP over the eastern TP are analyzed in detail. Conclusions are given in Section 6.

2. Materials and Methods

2.1. FY-4B/GIIRS ATP Products

The ATP products derived from FY-4B/GIIRS in this study were generated using a neural network algorithm developed by the National Satellite Meteorological Center (NSMC) [47]. This approach does not depend on the precision of the prior information and could provide more accurate products than the Dual-Regression method. The full disk ATP products' spatial and temporal resolution is 12km and 2 h, respectively. Although the observation period is 2 h, to ensure data quality, the first 90 min are the actual observation time, and the last half an hour is the GIIRS's self-check. FY-4B/GIIRS ATP products are stored in pressure vertical layers with 101 levels from 0.005 to 1100 hPa.

A QC Flag with four levels is used to mark the FY-4B/GIIRS ATP products (Table 1). In this paper, the ATP products marked with QC Flags 2 and 3 were excluded during the precision assessment. FY-4B/GIIRS ATP products have a Cloud Mask (CLM) in each detector; CLM equal to 0 means clear sky in this site while 1 indicates cloudy weather. Considering that satellite detection data in the infrared band are susceptible to cloud pollution [48], only products with CLM equal to 0, i.e., completely clear sky, are used.

Table 1. QC Flag and corresponding quality for FY-4B/GIIRS ATP products.

QC Flags	Quality
0	Perfect
1	Good
2	Bad
3	Do not use

The FY-4B/GIIRS ATP products were officially released for download on 17 January 2023. In this study, ATP products from 17 January 2023 to 17 January 2024, totaling 366 days, were selected for analysis and assessment.

2.2. RAOB ATP

The RAOB data come from the Department of Atmospheric Sciences of the University of Wyoming (https://weather.uwyo.edu/upperair/sounding.html, accessed on 5 November 2024). The detection range extends from the surface to 100 hPa in the upper troposphere, and meteorological elements include air pressure, temperature, mixing ratio, wind direction, wind speed, etc. Nine RAOB stations in the TP area are selected in this study, indicated by the red triangles in Figure 1a. Both terrain and land surface type play crucial roles

in determining the quality of satellite radiation retrieval [49]; the geolocation and land use categories for the nine selected RAOB stations are provided in Table 2, along with their precise geographical coordinates. The land use data are sourced from the Copernicus Global Land Service: land cover 100 m, collection 3, epoch 2019, covering the globe [50]. It can be seen from the table that the elevation of the nine stations ranges from 2295.2 m to 4507 m, of which the Nagqu has the highest topography, located in Tibet. As for the land use category of these stations, Dulan, Qamdo, Garze, and Yushu are classified as Grassland, while others are classified as Urban. According to Figure 1a, it can be found that all the RAOB stations are distributed in the eastern part of the TP. Before processing the radiosonde data, we conduct quality control to ensure the highest possible data quality.

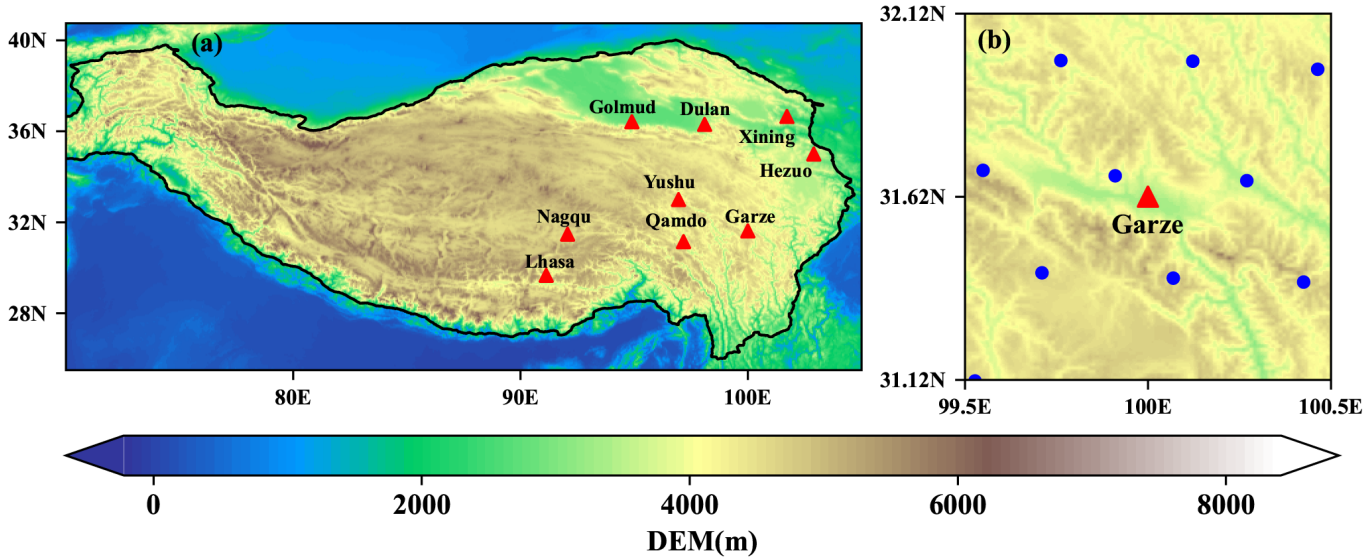

Figure 1. (**a**) Distribution map of the nine RAOB stations (red triangles) over the TP. (**b**) The FY-4B/GIIRS observation pixels (blue dots) for the Garze station in the MW method at 12 UTC on 17 January 2023. The color shading represents the elevation (units, m), and the red line in (**a**) indicates the border of the TP.

Table 2. Geolocation and land use type information of selected stations.

RAOB Station	Station ID	Location	Elevation (m)	Land Use
Xining	52866	101.72°E, 36.65°N	2295.2	Urban
Golmud	52818	94.90°E, 36.42°N	2807.6	Urban
Hezuo	56080	102.90°E, 35.00°N	2910.0	Urban
Dulan	52836	98.10°E, 36.30°N	3189.0	Grassland
Qamdo	56137	97.17°E, 31.15°N	3315.0	Grassland
Garze	56146	100.00°E, 31.62°N	3393.5	Grassland
Lhasa	55591	91.13°E, 29.67°N	3648.9	Urban
Yushu	56029	96.95°E, 33.00°N	3716.9	Grassland
Nagqu	55299	92.07°E, 31.48°N	4507.0	Urban

2.3. ERA5 ATP

The ERA5 ATP used in this study is obtained from the Copernicus Climate Change Service (https://cds.climate.copernicus.eu/datasets/reanalysis-era5-pressure-levels?tab=overview, accessed on 5 November 2024). ERA5 is the fifth-generation atmospheric reanalysis of the European Centre for Medium-Range Weather Forecasts (ECMWF), offering hourly and monthly reanalysis datasets with a horizontal resolution of 0.25° and vertical resolution across 37 pressure levels ranging from 1 hPa to 1000 hPa. The pressures of these 37 levels are 1 hPa, 2 hPa, 3 hPa, 5 hPa, 7 hPa, 10 hPa, 20 hPa, 30 hPa, 50 hPa, 70 hPa, 100 hPa, 125 hPa, 150 hPa, 175 hPa, 200 hPa, 225 hPa, 250 hPa, 300 hPa, 350 hPa, 400 hPa, 450 hPa,

500 hPa, 550 hPa, 600 hPa, 650 hPa, 700 hPa, 750 hPa, 775 hPa, 800 hPa, 825 hPa, 850 hPa, 875 hPa, 900 hPa, 925 hPa, 950 hPa, 975 hPa, and 1000 hPa. In this study, the daily ATP is derived with the arithmetic averaging of hourly datasets.

2.4. Methodology

The TP region is defined by the Integration dataset of the Tibet Plateau boundary [51], as shown in Figure 1a. To effectively and accurately evaluate the performance of FY-4B/GIIRS ATP in the eastern TP, it is essential to align the temporal and spatial positions of satellite data and atmospheric vertical pressure layers with the RAOB ATP. Temporally, the time difference in all ATP is limited to 1 h. Spatially, some researchers [38,52] used the matching window, which means the range of matchups is limited by using a given latitude and longitude grid centered on the RAOB station. Within the grid, satellite products are averaged and then matched into the RAOB ATP at the corresponding time. In this study, the distance of the matching window is limited to 0.5° × 0.5°, taking Garze as an example (Figure 1b). However, due to the removal of data from the cloud area, the number of available data is limited. So, the inverse distance weight (IDW) interpolation is also adopted for spatial matching. The IDW method is a simple approach that does not require extensive computations. It is considered one of the standard spatial interpolation techniques in geoinformation science [53–55]. Formally, the IDW method is used to estimate the unknown value $\hat{y}(S_0)$ in location S_0, given the observed y value at sampled location S_i as follows:

$$\hat{y}(S_0) = \sum_{i=1}^{n} \lambda_i y(S_i) \tag{1}$$

Essentially, the estimated value at S_0 is a linear combination of the weights λ_i and the observed y values at S_i where λ_i is typically defined as follows:

$$\lambda_i = \frac{d_{0i}^{-\alpha}}{\sum_{i=1}^{n} d_{0i}^{-\alpha}} \tag{2}$$

with

$$\sum_{i=1}^{n} \lambda_i = 1 \tag{3}$$

In Equation (2), the numerator d_{01} is the distance between S_0 and S_i with a power α. The denominator is the sum of all inverse distance weights for locations i ensuring that the sum of all λ_i for an unsampled point equals one (Equation (3)). The parameter α defines the weight's geometric form. A larger α enhances the distance decay effect, making it more sensitive to distance changes, while a smaller α leads to estimates that are averages of nearby S_i. Thus, larger α gives more weight to the nearest points and less to those further away [54].

Figure 2 compares the RMSE between FY-4B and RAOB and the number of effective data at nine RAOB stations for the two different matching methods. Except for Lhasa and Yushu, where the RMSE of the IDW method is slightly higher than that of the MW method, the RMSE for all other stations is lower when using the IDW method. The largest value occurs at Changdu station, reaching 1.53 K, while the differences at Golmud, Dulaan, and Naqu also exceed 1 K. For the remaining stations, the RMSE of the IDW method is marginally lower than that of the MW method. However, the count of effective data of the MW method is notably lower compared to that of the IDW method. Especially prominent at high-altitude sites such as Qamdo, Garze, Lhasa, Yushu, and Nagqu, the MW method yields effective data totals of approximately 60% or even lower compared to the IDW method. In summary, the IDW method not only allows for the acquisition of more valid data but also reduces the RMSE to some extent. Therefore, to obtain better statistical representativeness and more precise matching results, the effective dataset used in the evaluation should include as much data as possible. Therefore, in this study, the IDW

method was used for spatial matching. Radiosonde observation data typically consist of measurements taken at predefined isobaric levels (standard levels), totaling 24 layers [56].

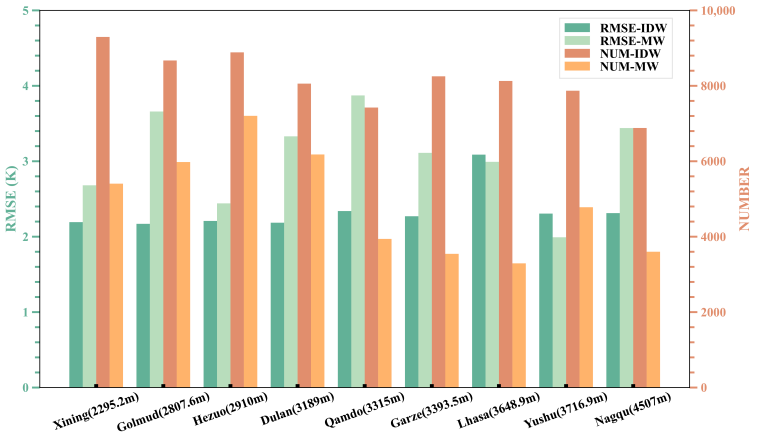

Figure 2. RMSE (green bars) and the number of effective data (orange bars) for the IDW and the MW method at nine RAOB stations.

However, due to the high altitude of our research area, the surface air pressure at the lowest-elevation Xining station is already above 750 hPa. Additionally, the top-level pressure in the University of Wyoming's RAOB data is 100 hPa. Therefore, the vertical study region ranges from 750 hPa to 100 hPa. However, this results in fewer vertical layers. To address this, we densified the vertical layers, ultimately obtaining the following vertical layers: 750, 700, 650, 600, 550, 500, 450, 400, 350, 300, 250, 200, 150, and 100 hPa. Given that both RAOB and FY-4B have dense vertical layers and that the temperature within the troposphere can be considered to vary linearly according to the lapse rate, the vertical matching method employed linear interpolation, which interpolated both RAOB and FY-4B ATP onto the same pressure layers.

Before comparing FY-4B/GIIRS ATP with ERA5 ATP, it is necessary to first compare ERA5 with RAOB to validate ERA5's representativeness ATP in the eastern TP. The specific approach involves using bilinear interpolation to interpolate ERA5 ATP onto the locations of the nine RAOB stations, followed by comparative validation, the same processing method as described earlier will be employed in the vertical direction. Subsequently, the FY4B ATP will be interpolated onto the ERA5 grid using the nearest neighbor method, facilitating subsequent comparisons. In the vertical direction, linear interpolation is utilized to interpolate FY-4B/GIIRS ATP onto the pressure layers of ERA5. Given the high altitude of the TP region where most locations have minimum pressure below 600 hPa, and uncertainties above 100 hPa are significant, this study focuses only on the data for 100 to 600 hPa, with 14 layers including 600, 550, 500, 450, 400, 350, 300, 250, 225, 200, 175, 150, 125, and 100 hPa.

Some objective statistical metrics are used in this study to evaluate the performance of ATP from FY-4B/GIIRS, RAOB, and ERA5: the mean bias (MB), the RMSE, the correlation coefficient (R), and the sample standard deviation (STD). These statistical metrics are expressed as follows:

$$MB = \frac{1}{n}\sum_{i=1}^{n}(x_i - y_i) \tag{4}$$

$$RMSE = \sqrt{\frac{1}{2}\sum_{i=1}^{n}(x_i - y_i)^2} \tag{5}$$

$$R = \frac{\sum_{i=1}^{n}(x_i - \overline{x})(y_i - \overline{y})}{\sqrt{\sum_{i=1}^{n}(x_i - \overline{x})^2 \sum_{i=1}^{n}(y_i - \overline{y})^2}} \tag{6}$$

$$STD = \sqrt{\frac{\sum_{i=1}^{n}(bias_i - \overline{bias})^2}{n-1}} \quad (7)$$

where x_i and $\overline{x}$ are the FY-4B/GIIRS ATP products and mean of FY-4B/GIIRS ATP products, respectively;y_i and $\overline{y}$ are the ATP of RAOB (or ERA5) and the mean of the ATP of RAOB (or ERA5), respectively; n is the total number of the observations; and the $bias_i$ and $\overline{bias}$ are the bias between FY-4B/GIIRS ATP and RAOB ATP (or ERA5).

3. The Quality of FY-4B/GIIRS ATP Under Clear and Cloudy Sky

As noted in Section 2.1, the quality of the FY-4B ATP products is marked with a four-level quality flag. Figure 3 depicts the percentages of the four different quality flags under clear and cloudy sky conditions in the TP region. Under clear sky conditions, over 70% of ATPs are categorized as "Perfect" or "Good", while the remaining 30% are deemed of lower quality and not utilized. However, under cloudy conditions, the percentage of "Perfect" decreases significantly to approximately 30%, while there is a slight growth in the percentages of "Good" and "Bad" compared to clear sky. Additionally, the percentage of "Do not use" increases from 22.8% under clear sky conditions to 39.2%.

Under clear sky conditions, FY-4B/GIIRS ATP products generally exhibit high usability. However, clouds significantly impact the quality of ATP products. Cloud contamination will significantly decrease the quality and usability of FY-4B/GIIRS ATP products.

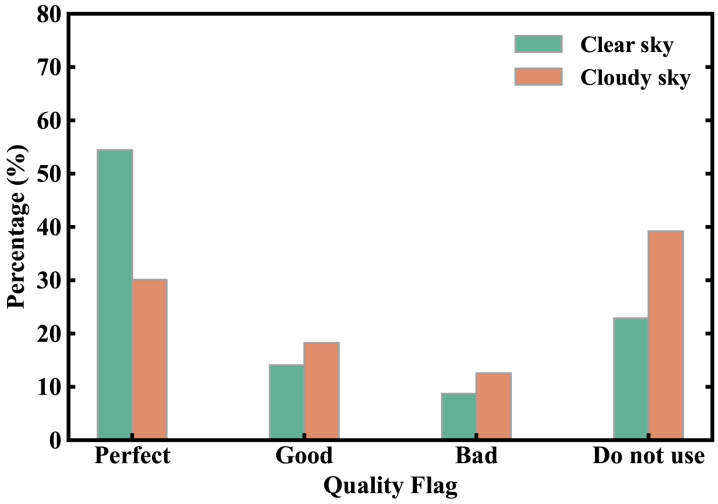

Figure 3. The percentages of the FY-4B/GIIRS ATP products quality flags during clear sky (green bars) and cloudy sky (orange bars).

4. Comparison Between RAOB ATP and FY-4B ATP

Figure 4 shows the vertical distribution of ATP observed by FY-4B/GIIRS (blue line) and RAOB. At 00 UTC (Figure 4a–i), FY-4B/GIIRS ATP is lower than RAOB on the surface layer in Golmud, Lhasa, and Nagqu stations while the other stations are generally higher. From the surface up to around 500 hPa, the FY-4B generally underestimates the air temperature compared to the RAOB observation, but such negative bias tends to decrease with elevation. As the pressure is lower than 500 hPa, almost none of the stations show a significant positive or negative bias, with bias fluctuating around 0 K, except the Lhasa station exhibits a relatively persistent underestimation with a maximum bias of −2 K. It is noticeable that the bias from 500 hPa to 150 hPa is relatively smaller than the lower layer in these RAOB stations. However, from 150 hPa to the uppermost layer, bias at all nine RAOB stations indicate an increasing trend towards positive bias, with Lhasa, Yushu, and Nagqu showing the most notable growth. Particularly, at the Nagqu, the bias has already reached around 4K at 100 hPa.

At 12 UTC (Figure 4j–r), apart from the Lhasa, the vertical trend of bias at the other eight stations is generally similar to that at 00 UTC, but there are some differences. Specifi-

cally, all nine stations exhibit negative bias at the surface, with higher-elevation stations such as Qamdo (Figure 4n), Garze (Figure 4o), Lhasa (Figure 4p), Yushu (Figure 4q), and Nagqu (Figure 4r) showing more severe underestimation compared to 00UTC. From the surface to 500hPa, all stations show a decreasing trend in bias values. From 500 hPa to the uppermost layer, except for the Lhasa station, the variation in bias at the other stations is similar to that at 00UTC, but with smaller fluctuations in bias. The Lhasa station exhibits significant differences in bias compared to 00UTC, characterized by consistent underestimation throughout the layers. Specifically, there is noticeable underestimation at the surface and near-surface, with bias approaching approximately −8K at the surface and decreasing with height, reaching a minimum around 300 hPa, followed by a slight boost in underestimation as height increases further, reaching around −2K at 150 hPa.

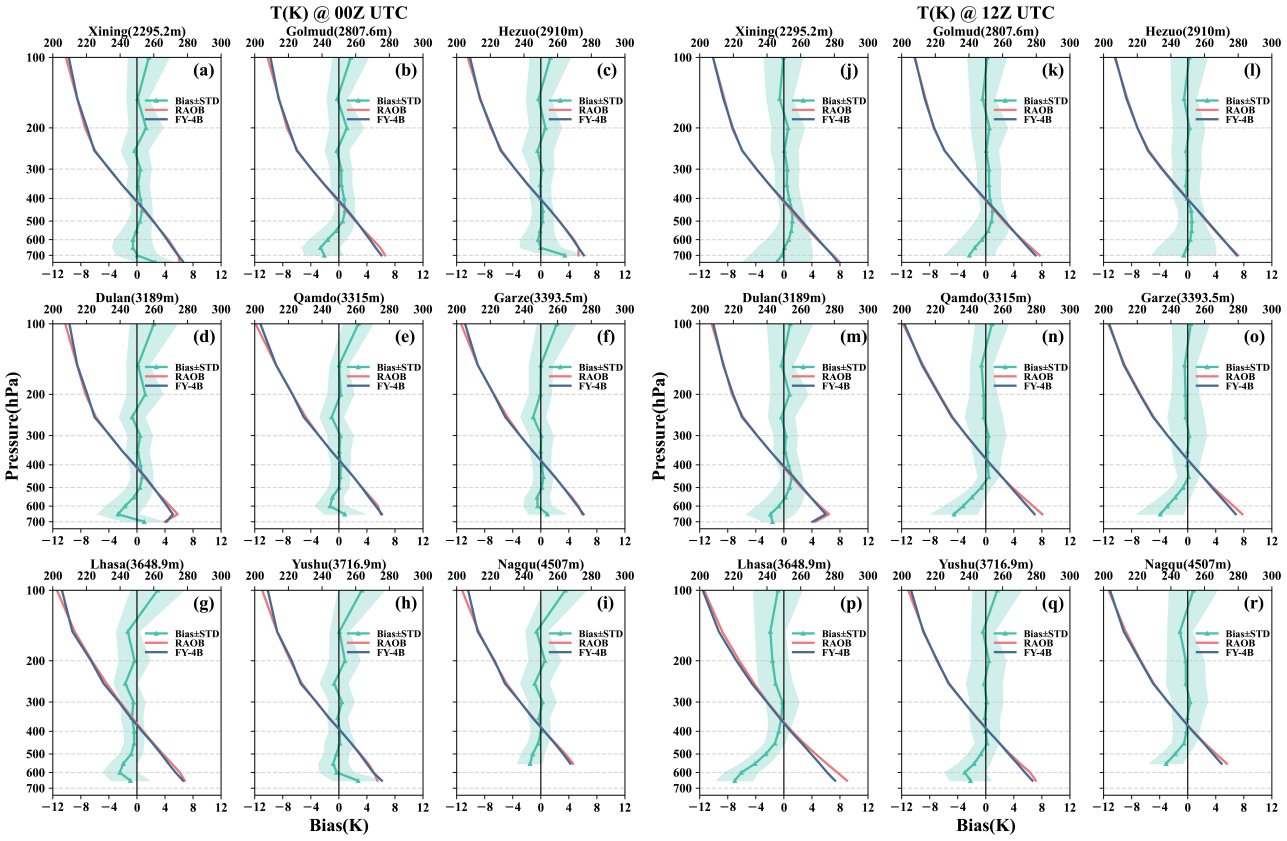

Figure 4. The average ATP observed by FY-4B/GIIRS (blue line) and RAOB (orange line) and the average bias of FY-4B/GIIRS referring to RAOB (cyan line with triangles) for (**a**–**i**) 00 UTC and (**j**–**r**) 12 UTC. The light cyan shading accompanied with the bias line indicates one standard variation of the bias.

From the perspective of STD, at or above 150 hPa, the STD for all nine stations shows an increase at both 00UTC and 12 UTC, indicating slightly higher instability compared to other pressure levels. Between 500 and 150 hPa, although some STD is present, the small value of the bias means that even with the addition of STD, the bias still fluctuates within a narrow range. Near the surface, STD does not significantly differ from the mid-troposphere, except for the Xining (Figure 4j), Golmud (Figure 4k), and Hezuo (Figure 4l) stations at 12 UTC. Overall, both at 00 UTC and 12 UTC, the vertical variation in STD over the nine RAOB stations remains relatively stable, all within 5 K, with no abrupt changes. This reflects the higher stability and consistency of FY-4B ATP products.

Having analyzed the overall distribution of ATP from FY-4B/GIIRS and RAOB, we further investigate their correlations with the RAOB ATP in the entire atmospheric layers. Figure 5 presents the comparison results of ATP between FY-4B and RAOB at nine stations.

Additionally, the regression equation (red line), R, total data number (N), MB, and RMSE are also presented in the figure. Overall, the fitting between FY-4B ATP and RAOB ATP is good, with data points distributing roughly around the 1:1 line, showing no significant deviations or dispersion. This is reflected in the R, with all nine stations having R greater than 0.99, indicating an excellent correlation between ATP from FY-4B and RAOB. Furthermore, based on the density of data point distribution, the majority of data points are concentrated near the 1:1 line, further demonstrating the good consistency between the two ATP products. This is a positive outcome, indicating the presence of consistency and similarity between FY-4B and RAOB ATP.

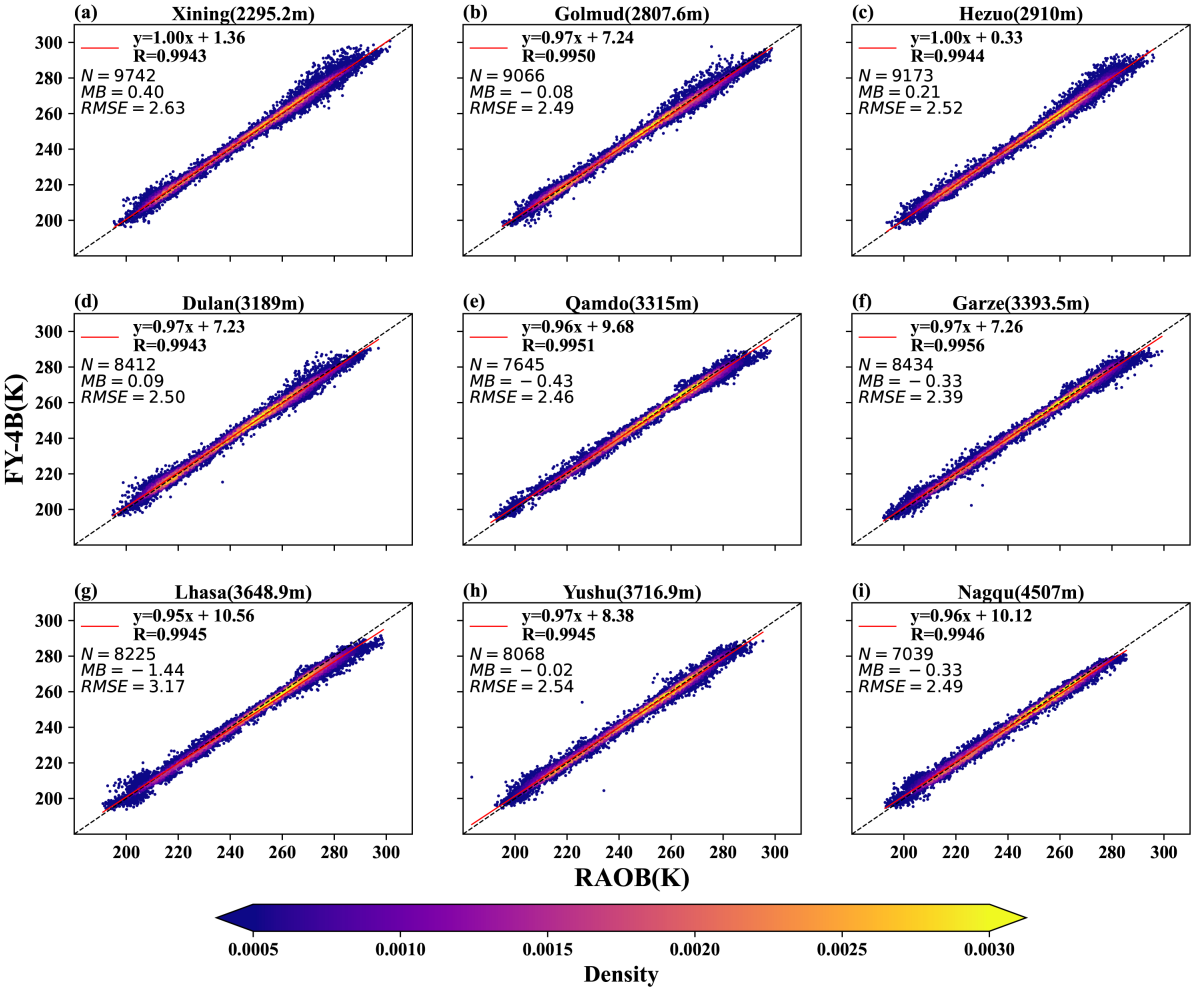

Figure 5. Scatter plot of FY-4B/GIIRS ATP versus the RAOB ATP (black dashed line represents the 1:1 line, red line represents regression line). (**a**–**i**) represent nine RAOB stations arranged in order of elevation from lowest to highest.

As the elevation of the station position increases, there is an observable decline trend in the number of effective data points, primarily attributed to the reduction in lower-level data resulting from the topographic elevation. However, despite its elevation being located between Dulan (Figure 5d) and Garze (Figure 5f), Qamdo (Figure 5e) demonstrates a lower total data point volume compared to the higher-elevation Lhasa (Figure 5g) and Yushu (Figure 5h). This suggests a higher occurrence of lower-quality FY-4B ATP data at Qamdo.

From a quantitative analysis perspective, among the nine stations, Xining (Figure 5a), Hezuo (Figure 5c), and Dulan (Figure 5d) exhibit MB values greater than 0, indicating that FY-4B tends to overestimate temperatures in these three stations and their surrounding areas to varying degrees. Conversely, in the remaining six stations and their surrounding areas, the bias is predominantly underestimated. The largest positive bias occurs at the

Xining station (Figure 5a), which has the lowest elevation among all nine stations, with a value of 0.40K. The largest negative bias is observed at the Lhasa station (Figure 5g), with an MB value of −1.44K. For the RMSE, the highest value is observed at the Lhasa station (Figure 5g), reaching 3.17K, while the lowest one is recorded at the Garze station (Figure 5f), at 2.39 K. With a relatively small range of RMSE variation, it indicates that FY-4B/GIIRS ATP demonstrates good spatial consistency in quality control.

5. Spatiotemporal Evaluation of FY-4B/ATP for a Whole Year

The relationships between ERA5 ATP and nine RAOB ATP are depicted in Figure 6. It can be visually observed that compared to FY-4B, ERA5 exhibits better consistency with RAOB since scatters at nine RAOB stations show a tighter distribution. The R at all stations except Hezuo (Figure 6c), Garze (Figure 6f), Lhasa (Figure 6g), and Yushu (Figure 6h) are 0.999 or higher. Although the R at these four stations is slightly lower, at 0.9987, 0.9989, 0.9984, and 0.9983, respectively, compared to 0.999, the comparison with FY-4B/GIIRS ATP (Figure 6c,f,g,h) still shows improvements. The MB at all nine stations suggests that ERA5 ATP tends to underestimate temperature. From the graphs, it is evident that the majority of bias originates from temperatures above 260 K, indicating a more pronounced underestimation near the surface layer.

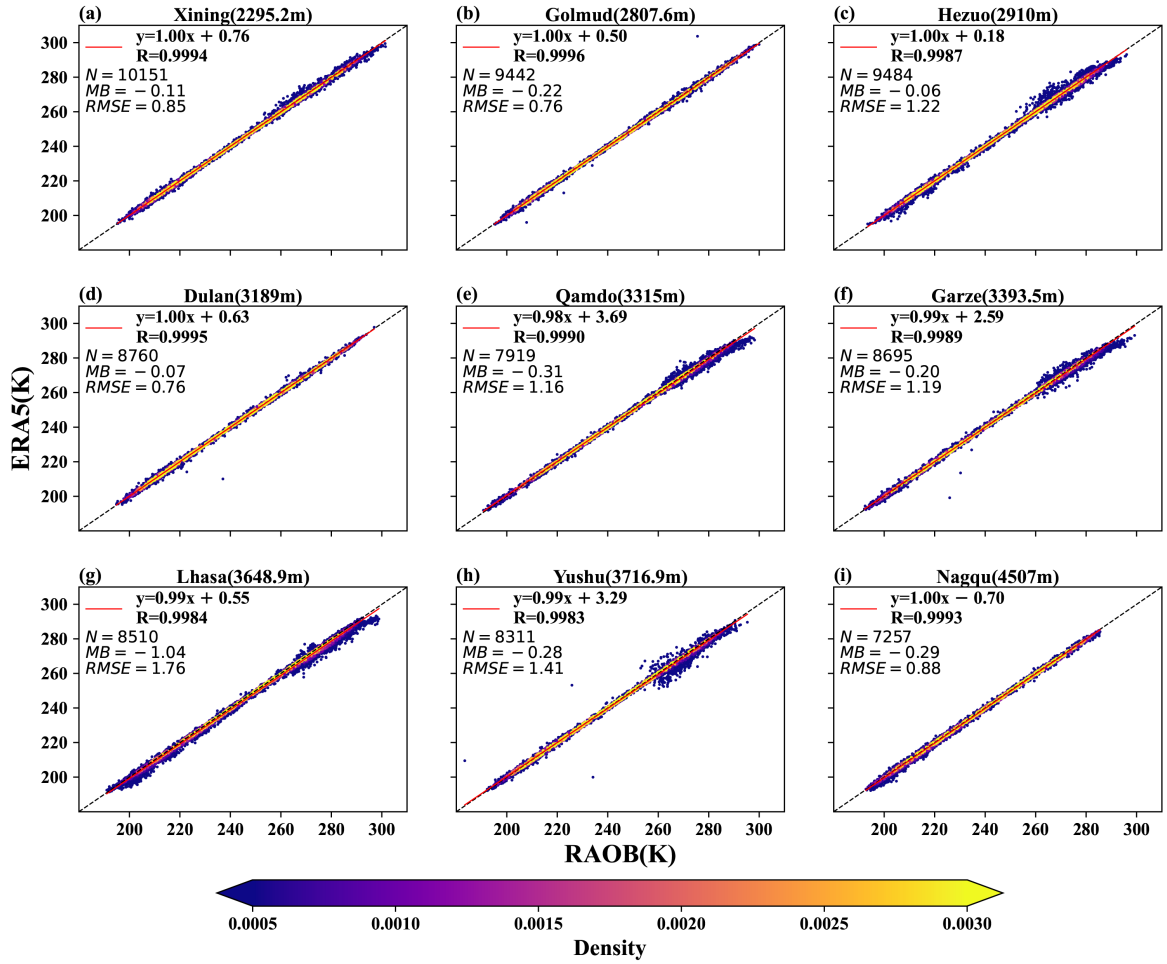

Figure 6. Same as Figure 5, but for ERA5 ATP versus the RAOB ATP. (**a**–**i**) represent nine RAOB stations arranged in order of elevation from lowest to highest.

Although the comparison between ERA5 and RAOB reveals certain bias in ERA5 ATP, overall, ERA5 ATP still maintains good consistency with RAOB ATP, with relatively small

bias values. Therefore, it can be considered sufficiently representative for evaluating the performance of FY-4B/GIIRS ATP in the eastern TP.

As shown in Figure 7a, due to the zenith angle of FY-4B/GIIRS being too large in the western TP, where deformation rates increase with the satellite zenith angle and reach up to three times the Sub-Satellite point deformation at angles exceeding 60°, there is a significant difference in data availability between the eastern and western TP [57,58]. This could cause a significant decrease in the representativeness, reliability, and availability of data among the western TP during spatial analysis.

The annual mean temperature of the entire region after interpolation (Figure 7b) reveals a distinct arc around 85–95°E, which is the borderline of the zenith angle of 60°. The continuity of data on the western side of the arc is poor, and its reliability cannot be verified. To retain as much valid data as possible, the intersection points of the arc and the north-south boundaries of the TP, denoted as points A (87°E, 27.5°N) and B (95.5°E, 39.75°N), are selected to establish a line (Figure 7b). Subsequently, the observations at the east of the red line in Figure 7b are analyzed (Figure 7c), as shown in Figure 7c.

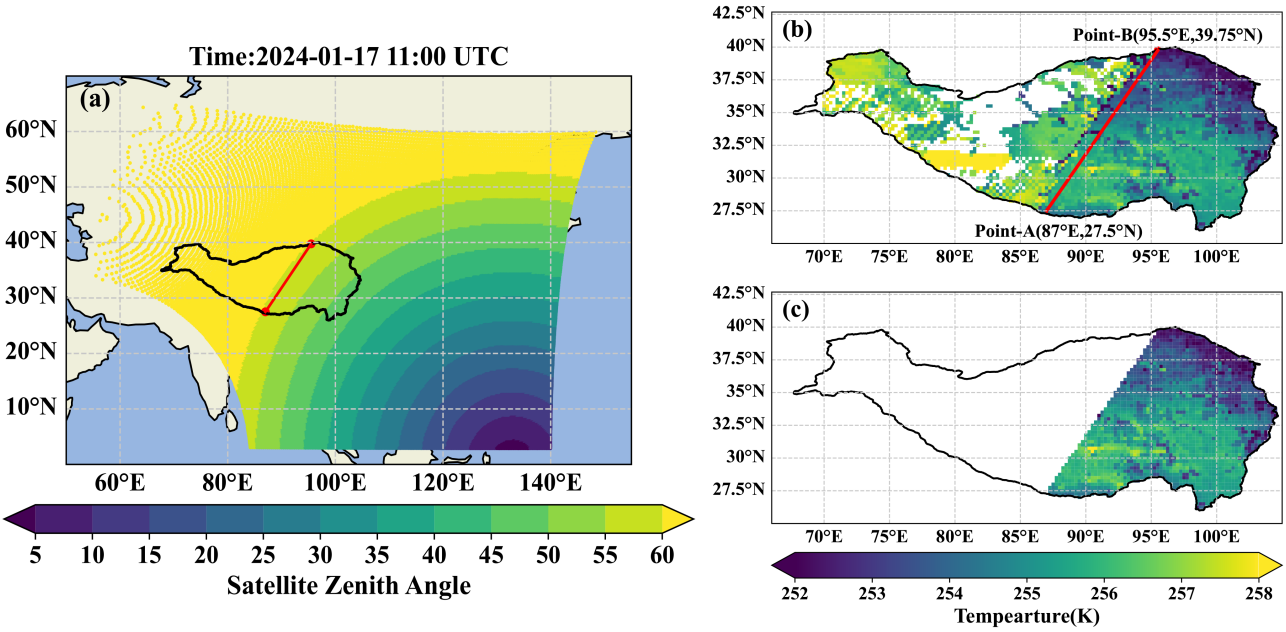

Figure 7. (**a**) Satellite zenith angle (shaded, degree) of FY-4B/GIIRS at 11:00 UTC on 17 January 2024 and the annual mean troposphere temperature (**b**) before and (**c**) after filtering based on the satellite zenith angle of 60° as the red line shown in (**b**). The black line in (**a**–**c**) indicates the TP region. Points A and B in (**b**) are the intersection points of the contour line of 60° and the borderline of the TP region in (**a**).

As depicted in Figure 8, the annual average tropospheric temperature is dominated by positive bias orientating from south to north of the eastern TP, with a bias over 0.25 K. The largest bias is located in the central region of the study area (indicated by the blue box in Figure 8a), where the bias ranges from 0.5 K to 0.75 K with a maximum of up to 0.84 K. While the temperature bias over the southeastern and southwestern parts of the study area exhibits as slightly negative, it is majorly less than −0.25 K.

To further investigate the vertical characteristics of bias, we select the region with the most pronounced positive bias (indicated by the blue box in Figure 8a). The pattern in Figure 8b suggests that FY-4B/GIIRS tends to overestimate temperature above 150 hPa, with the most significant bias at 100 hPa, where the value of bias exceeds 2 K. Bias at and below 150 hPa is relatively slighter, staying within ±2 K. At 150 hPa, the bias is relatively smaller, at only 0.16K. The above analysis suggests that the spatial average bias in this region ultimately shows positive values because the positive bias in the upper layers contributes more to the bias than the negative bias in the lower layers. The vertical distribution of

STD is uniform, with an average value of 1.36 K across the entire layer. The maximum STD occurs at 100 hPa, reaching 2.23 K, while the minimum value is at 400 hPa, at 0.92 K. This indicates that the overall dispersion of bias is low, with few outliers, suggesting good quality control of the ATP from FY-4B.

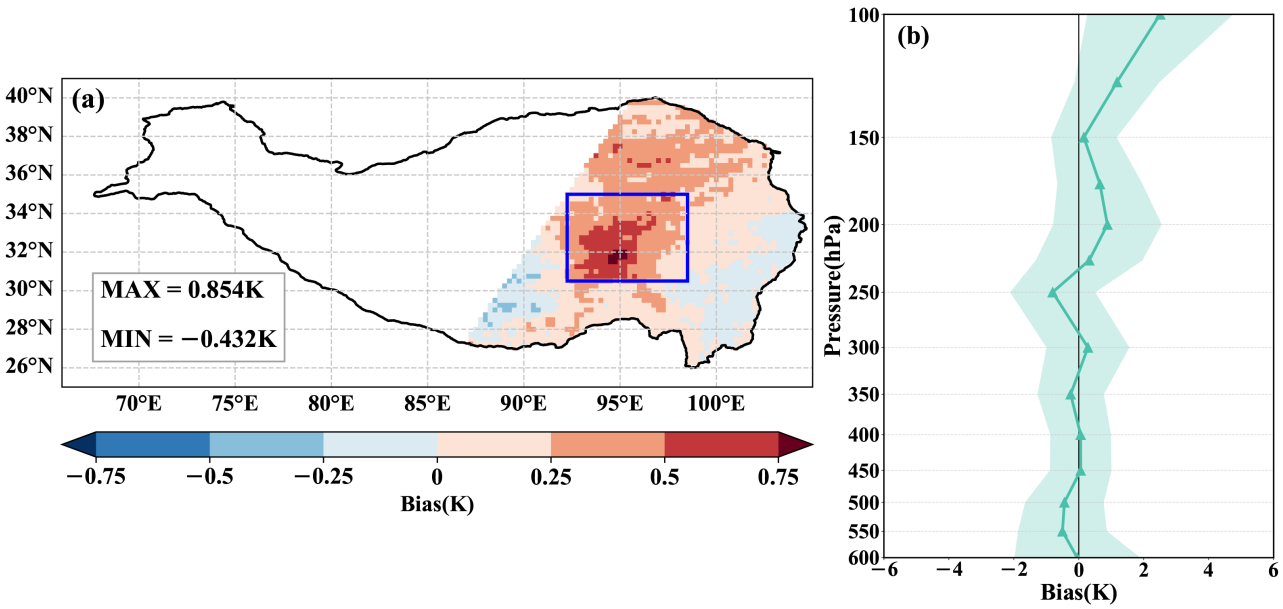

Figure 8. The spatial distribution of annual mean temperature bias between FY-4B/GIIRS and ERA5 ATP: (**a**) horizontal distribution of troposphere (600–100 hPa) averaged bias and (**b**) vertical distribution of regional averaged bias for the blue box in (**a**). The shading in (**b**) indicates one STD range of the bias.

Notably, the vertical bias distribution pattern shown in Figure 7b is similar to the vertical bias distribution pattern at 00 UTC between the FY-4B and RAOB (Figure 4a–i, above 600 hPa) discussed earlier. This similarity indicated that the ATP bias of FY-4B exhibits good spatial consistency in the eastern TP region. This provides data support for the subsequent use of the product and bias correction.

As shown in Figure 9, the density distribution indicates that most data points across the four seasons are clustered near the 1:1 line, suggesting a good consistency between FY-4B/GIIRS ATP and ERA5 ATP. The correlation coefficient R for all four seasons is greater than 0.99, with summer (Figure 9c) achieving the highest R of 0.9994, while autumn (Figure 9d) has the lowest at 0.9978. Except for summer, where the MB is negative at −0.29 K, the MB for the other three seasons is positive. The largest positive MB occurs in spring (Figure 9b) at 0.47 K, while the smallest positive MB is in autumn at only 0.03 K, and winter (Figure 9a) has an MB of 0.33 K. From the perspective of RMSE, although autumn has the smallest MB, it exhibits the largest RMSE at 1.55 K. This suggests that autumn may contain comparable positive and negative bias that offset each other in the MB calculation. Winter and spring have very similar RMSE values of 1.17 K and 1.19 K, respectively, while summer has the smallest RMSE at 1.00 K.

Figure 10 gives the horizontal distribution of bias in different seasons. We note that the pattern of the bias over the eastern TP region is similar in winter, spring, and autumn, but their values show some differences. In spring (Figure 10b), most of the areas are dominated by positive bias, with the highest value reaching 1.52 K, and within the rectangular region, most bias exceeds 0.75 K. During the winter (Figure 10a), areas with positive bias are fewer compared to the spring, but the eastern TP still predominantly exhibits positive bias, with the highest value being 1.08 K, which is lower than in the spring, and most bias exceeds 0.5 K within the rectangular region. However, in the northern part of the rectangular, the bias slightly increases compared to the spring. Additionally, in areas with a negative

bias, the values also slightly increase, with the maximum negative bias reaching −1.18 K. Although the pattern is similar to winter and spring, the values of bias are relatively lower in autumn (Figure 10d). Its highest positive bias and the lowest negative bias are 0.79 K and −0.34 K, respectively, indicating a significant decrease compared to winter and spring. In summer, the bias distribution pattern differs significantly from the other three seasons, shifting from a predominantly positive bias to a negative bias-dominated pattern. Although most areas exhibit negative bias, there are still some regions with positive bias. These areas, where positive bias persists, are consistent with regions of significant positive bias observed in the other seasons.

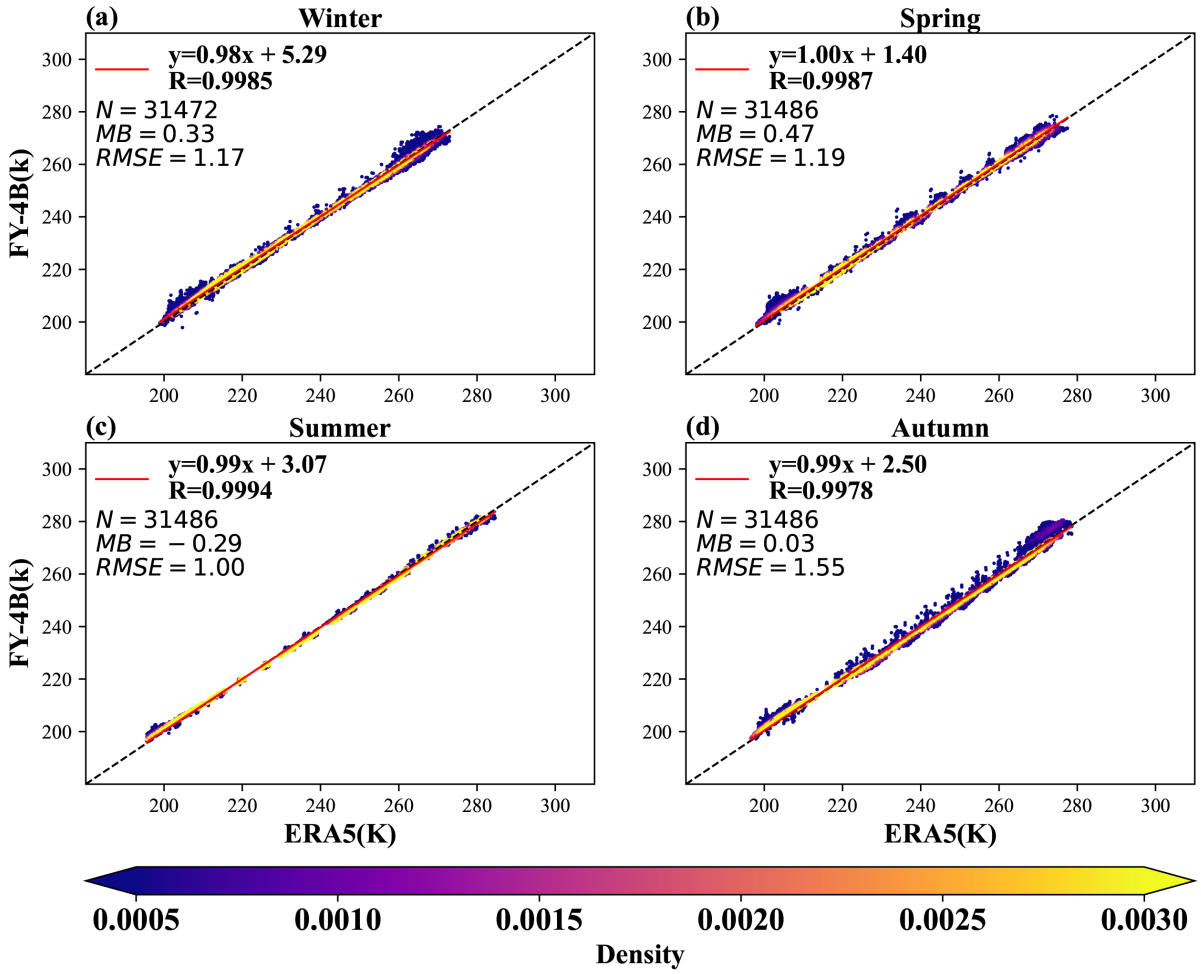

Figure 9. Scatter plot of seasonal average FY-4B/GIIRS ATP versus ERA5 ATP for each of the four seasons among the eastern TP, the black dashed line represents the 1:1 line, and the red line represents the regression line. (**a**–**d**) correspond to winter, spring, summer, and autumn, respectively.

We also analyze the vertical distribution of bias within the rectangular region for each of the four seasons (Figure 11). The largest positive bias across all four seasons occurs at 100 hPa, with spring (Figure 11b) showing the highest bias at 3.21 K, followed by winter (Figure 11a) at 2.34 K. The bias at 100 hPa in summer (Figure 11c) and autumn (Figure 11d) is comparatively smaller, measuring 1.97 K and 2.07 K, respectively. From 100 hPa to 150 hPa, the positive bias for all four seasons decreases as the pressure increases, approaching 0 K at 150 hPa. A positive bias predominates from 150 hPa to 200 hPa in winter, spring, and autumn. Within this pressure range, the peak positive bias for winter and spring occurs at 200 hPa, with values of 2.04 K and 1.50 K, respectively. In autumn, the maximum positive bias in this range is observed at 175 hPa, with a value of 0.91 K. At 250 hPa, significant negative bias is observed in winter and autumn, with values of −0.81 K and −1.06 K,

respectively, while no significant bias is noted in spring. In winter, there is a noticeable positive bias at 300 hPa, with a value of 1.11 K, while spring and autumn exhibit a smaller positive bias. Between 350 hPa and 450 hPa, winter and autumn show no significant bias, whereas spring presents a slight positive bias. From 450 hPa to 600 hPa, winter and spring exhibit negative bias. The largest negative bias in winter occurs at 500 hPa, with a value of −1.44 K, while in spring, the largest negative bias is observed at 600 hPa, recorded at −1.22 K. In autumn, no significant bias is present within this pressure layer. The vertical distribution of bias in summer exhibits a pattern distinct from that of other seasons. Aside from small positive bias at 450 hPa and 500 hPa, negative bias are present from 150 hPa to 600 hPa, with the largest negative bias occurring at 250 hPa, recorded at −1.03 K.

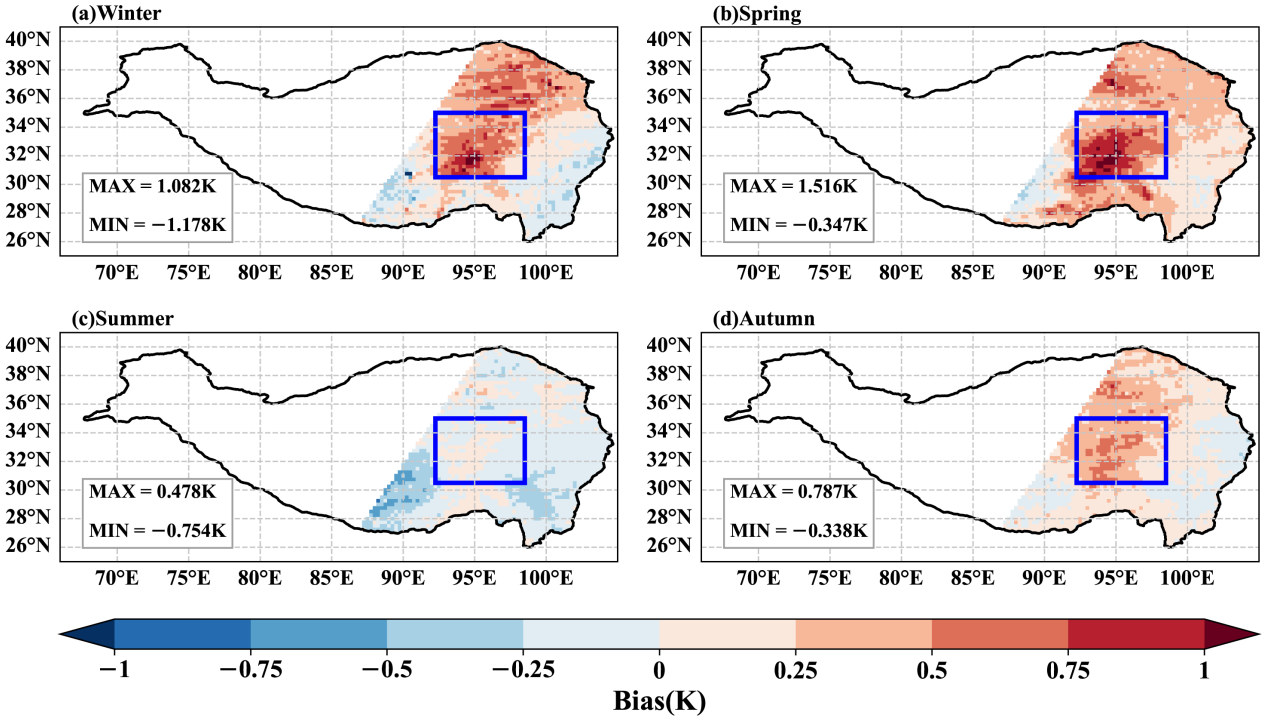

Figure 10. The horizontal distribution of annual mean troposphere (600–100 hPa) averaged temperature bias between FY-4B/GIIRS and ERA5 ATP. (**a**–**d**) correspond to winter, spring, summer, and autumn, respectively.

Moreover, as can be seen from Figure 11, the negative bias in the lower layers (below 450 hPa) during the winter and spring is also more pronounced than in the summer and autumn. This indicates that the bias across the entire layers exhibits a synchronous variation trend, meaning that as the positive bias in the mid-to-upper layers increases, the negative bias in the lower layers also increases simultaneously. In the autumn season (Figure 11d), the vertical pattern of bias is similar to the pattern of spring (Figure 11a) and winter (Figure 11b), but the values of bias are slight. In the summer (Figure 11c), although there is a remarkable difference in the vertical bias pattern, with predominantly negative bias overall, positive bias is still present in the upper layers (above 150 hPa). The average STD of vertical bias for the four seasons is 1.19 K, 1.45 K, 0.90 K, and 0.96 K, respectively. Similarly, the STD for winter and spring is higher than that for summer and autumn.

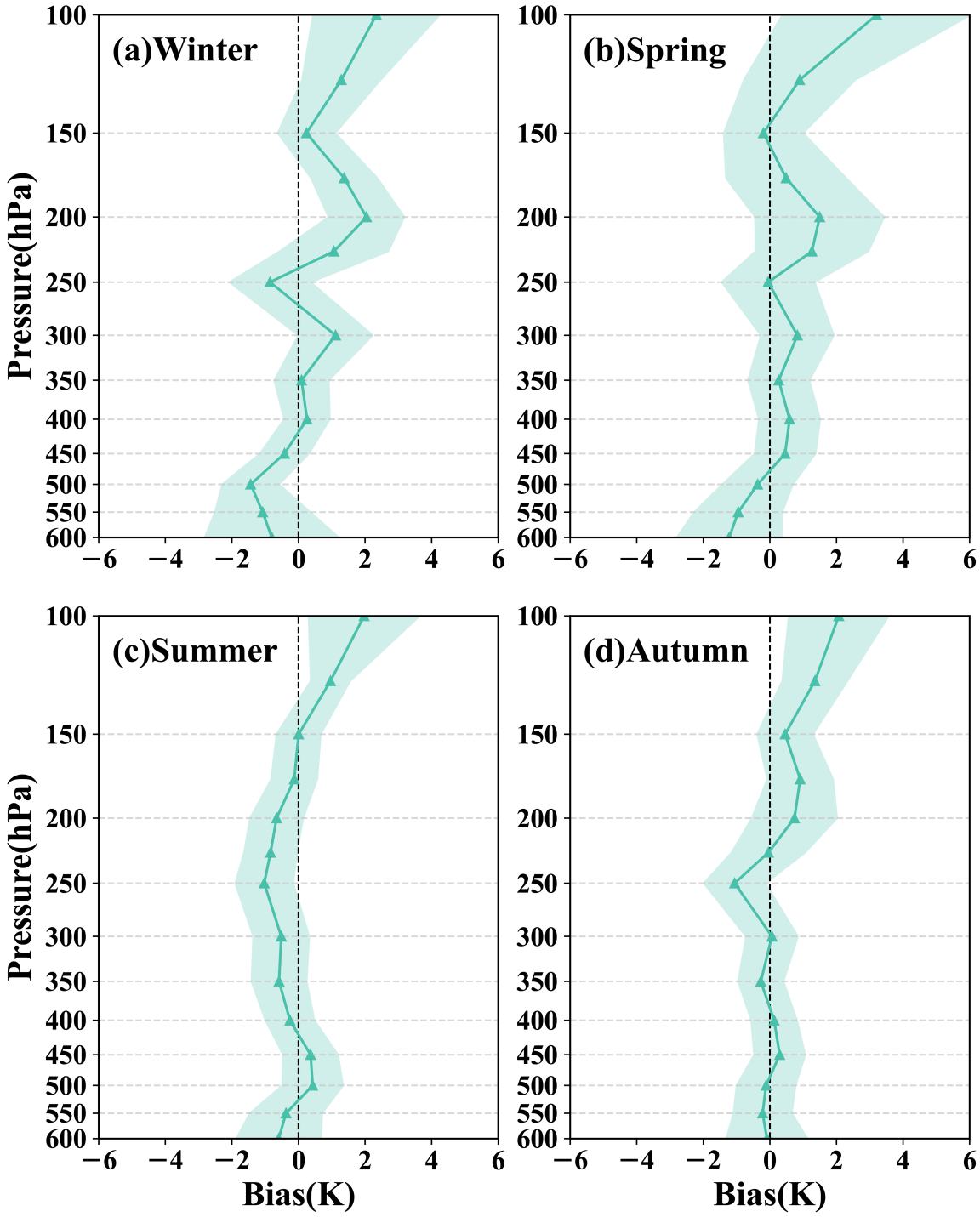

Figure 11. The vertical distribution of annual mean regional averaged temperature bias between FY-4B/GIIRS and ERA5 ATP for the blue box in Figure 8a. The shading indicates one STD range of the bias. (**a**–**d**) correspond to winter, spring, summer, and autumn, respectively.

6. Summary and Discussions

Due to the complex terrain and sparse population in the TP region, it is hard to obtain exact and wide-ranging atmospheric temperature profiles from conventional observations. At present, the Geostationary Interferometric Infrared Sounder (GIIRS) onboard the FY-4 series satellite can effectively eliminate this deficiency. Based on the ATP data from RAOB, ERA5 and the latest FY-4B/GIIRS products, this study uses various spatiotemporal

matching ways to minimize the spatiotemporal differences between different data and investigates the performance of FY-4B/GIIRS ATP products over the eastern TP region.

Our research demonstrates the product quality of ATP from FY-4B/GIIRS is closely related to the cloud conditions. Under clear sky conditions, the percentage of ATP with "Perfect" and "Good" QC Flags is 68.45%. Under cloudy conditions, however, the proportion of "Perfect" and "Good" declines to 48.3%, representing a reduction of approximately 20% compared to clear sky conditions. This results in a distinct decrease in the availability of products when there is substantial cloud cover over the TP region. FY-4B/GIIRS ATP exhibits great consistency with RAOB ATP, with an average RMSE of only 2.58 K, ranging from 2.39 K to 3.17 K. The bias shows slight variations among different RAOB sites and between day and night, especially near the surface and in the upper troposphere. The dispersion of bias across various sites is also relatively uniform. In the lower layers, FY-4B/GIIRS temperatures are generally lower than those from RAOB, while they are higher than RAOB in the upper layers. The bias is slight in the middle layers. Bias does not exhibit a significant correlation with altitude or land use type, suggesting that altitude and land use type may not be the primary factors affecting the detection and retrieval performance of FY-4B/GIIRS in the eastern TP. Moreover, the bias of FY-4B/GIIRS ATP demonstrates different characteristics in different regions, but overall, overestimation is predominant over the eastern TP, especially in winter and spring. This may be related to snow cover, as the spatial distribution pattern of annual average bias correlates to some extent with the spatial distribution of annual snow days in the TP region according to Huang et al. [59]. Snow cover directly impacts the albedo and land surface emissivity (LSE), which are closely related to satellite detection results.

However, due to the limitation of satellite zenith angle, only data from the eastern part of the TP are available for evaluation and analysis in this study, limiting a comprehensive analysis of the quality of FY-4B/GIIRS ATP products across the entire TP. Consequently, the finding cannot be generalized to the western TP area. However, with FY-4B drifting from 133°E to 105°E on 5 March 2024 and replacing FY-4A as the main operational system (http://www.nsmc.org.cn/nsmc/cn/satellite/FY4B.html, accessed on 5 November 2024), the satellite zenith angle in the TP region would decrease. As a result, complete detection data for the TP region will be obtainable. Nonetheless, this study systematically evaluates the quality of FY-4B/GIIRS ATP products accumulated over one year in the eastern TP region. It unearths the potential application value of FY-4B in the TP region and provides a certain preliminary research foundation for the subsequent related studies.

Author Contributions: Conceptualization, Y.W., X.W. and H.-L.R.; methodology, Y.W., X.W., H.Z. and H.-L.R.; software, Y.W. and X.W.; validation, Y.W., X.W.; formal analysis, Y.W. and X.W.; investigation, Y.W., X.W., H.Z., H.-L.R. and K.Y.; resources, H.Z. and H.-L.R.; data curation, Y.W. and H.Z.; writing—original draft preparation, Y.W.; writing—review and editing, X.W., H.Z., H.-L.R. and K.Y.; visualization, Y.W.; supervision, X.W., H.-L.R.; funding acquisition, X.W. and H.Z. All authors have read and agreed to the published version of the manuscript.

Funding: This research was funded by the Second Tibetan Plateau Scientific Expedition and Research Program (Grant number 2019QZKK010203), the Science and Technology Program of Xizang Autonomous Region (Grant number XZ202402ZD0006), the Sichuan Science and Technology Program (Grant number 2024YFFK0411), the Joint Research Project for Meteorological Capacity Improvement (Grant number 23NLTSZ003), the Youth Innovation Team of China Meteorological Administration "Climate change and its impact in the Tibetan Plateau" (Grant number CMA2023QN16).

Data Availability Statement: The FY-4B/GIIRS ATP products are provided by the FENGYUN Satellite Data Center from the website at http://satellite.nsmc.org.cn/portalsite/default.aspx/ (accessed on 5 November 2024). The RAOB data is provided by the University of Wyoming Atmospheric Science Radiosonde Archive from the website at https://weather.uwyo.edu/upperair/bufrraob.shtml (accessed on 5 November 2024). The ATP from re-analysis data is calculated from the ERA5 hourly data from the website at https://cds-beta.climate.copernicus.eu/datasets/reanalysis-era5-pressure-levels?tab=download (accessed on 5 November 2024).

Acknowledgments: We really appreciate National Satellite Meteorological Center for providing the FY-4B/GIIRS ATP products. We also thank the Department of Atmospheric Sciences of University of Wyoming for providing the Radiosonde observations datasets. We also appreciate ECMWF for providing the ERA5 reanalysis datasets.

Conflicts of Interest: The authors declare no conflicts of interest.

References

1. Cintineo, R.M.; Otkin, J.A.; Jones, T.A.; Koch, S.; Stensrud, D.J. Assimilation of Synthetic GOES-R ABI Infrared Brightness Temperatures and WSR-88D Radar Observations in a High-Resolution OSSE. *Mon. Weather Rev.* **2016**, *144*, 3159–3180. [CrossRef]
2. Ma, Y.; Liu, J.; Mamtimin, A.; Aihaiti, A.; Xu, L. Validation of FY-4A Temperature Profiles by Radiosonde Observations in Taklimakan Desert in China. *Remote Sens.* **2023**, *15*, 2925. [CrossRef]
3. Wang, G.; Han, W.; Yuan, S.; Wang, J.; Yin, R.-Y.; Ye, S.; Xie, F. Retrieval of High-Frequency Temperature Profiles by FY-4A/GIIRS Based on Generalized Ensemble Learning. *J. Meteorol. Soc. Jpn. Ser. II* **2023**, *102*, 241–264. [CrossRef]
4. Wang, H.; Zhou, H.F.; Wang, C.; Xia, Y.N. Accuracy validation of FY-4A temperature profile based on microwave radiometer and radiosonde. *Appl. Meteor. Sci.* **2023**, *34*, 295–308. [CrossRef]
5. Yao, T.D.; Xue, Y.K.; Chen, D.L.; Chen, F.H.; Thompson, L.; Cui, P.; Koike, T.; William, K.-M.; Lettenmaier, D.; et al. Recent Third Pole's Rapid Warming Accompanies Cryospheric Melt and Water Cycle Intensification and Interactions between Monsoon and Environment: Multidisciplinary Approach with Observations, Modeling, and Analysis. *Bull. Am. Meteorol. Soc.* **2019**, *100*, 423–444. [CrossRef]
6. Spicer, R.A.; Farnsworth, A.; Su, T. Cenozoic topography, monsoons and biodiversity conservation within the Tibetan Region: An evolving story. *Plant Divers.* **2020**, *42*, 229–254. [CrossRef]
7. Ding, W.H.; Ree, R.A.; Spicer, R.A.; Xing, Y.-W. Ancient orogenic and monsoon-driven assembly of the world's richest temperate alpine flora. *Science* **2020**, *369*, 578–581. [CrossRef]
8. He, S.L.; Ding, L.; Xiong, Z.Y. A distinctive Eocene Asian monsoon and modern biodiversity resulted from the rise of eastern Tibet. *Sci. Bull.* **2022**, *67*, 2245–2258. [CrossRef]
9. Qi, W.; Liu, S.H.; Zhou, L. Regional differentiation of population in Tibetan Plateau: Insight from the "Hu Line". *Acta Geogr. Sin.* **2020**, *75*, 255–267.
10. Zhao, P.; Xu, X.D.; Chen, F.; Guo, X.L.; Zheng, X.D.; Liu, L.P.; Hong, Y.; Li, Y.Q.; La, Z.; Peng, H. The Third Atmospheric Scientific Experiment for Understanding the Earth–Atmosphere Coupled System over the Tibetan Plateau and Its Effects. *Bull. Amer. Meteor.* **2018**, *99*, 757–776. [CrossRef]
11. Tao, S.Y.; Luo, S.W.; Zhang, H.C. The Qinghai-Xizang Plateau Meteorological Experiment (Qxpmex) May–August 1979. In Proceedings of the International Symposium on the Qinghai-Xizang Plateau and Mountain Meteorology, Lhasa, China, 20–24 August 1986; pp. 3–13.
12. Ma, Y.M.; Kang, S.C.; Zhu, L.P.; Xu, B.Q.; Tian, L.D.; Yao, T.D. Roof of the World: Tibetan observation and research platform. *Bull. Am. Meteorol. Soc.* **2008**, *89*, 1487–1492.
13. Zhang, R.H.; Koike, T.; Xu, X.D.; Ma, Y.M.; Yang, K. A China-Japan Cooperative JICA Atmospheric Observing Network over the Tibetan Plateau (JICA/Tibet Project): An Overviews. *J. Meteorol. Soc. Jpn. Ser. II* **2012**, *90*, 1–16. [CrossRef]
14. He, J. Study on the assimilation program of high-resolution regional information on the Tibetan Plateau. Ph.D. Thesis, Nanjing University of Information Science & Technology, Nanjing, China, 16 June 2016.
15. Strow, L.L.; Hannon, S.E.; De Souza-Machado, S.; Motteler, H.E.; Tobin, D. An overview of the AIRS radiative transfer model. *IEEE Trans. Geosci. Remote. Sens.* **2003**, *31*, 303–313. [CrossRef]
16. Pougatchev, N.; August, T.; Calbet, X.; Hultberg, T.; Oduleye, O.; Schlüssel, P.; Stiller, B.; Germain, K.S.; Bingham, G. IASI temperature and water vapor retrievals—Error assessment and validation. *Atmos. Chem. Phys.* **2009**, *9*, 6453–6458. [CrossRef]
17. Li, J.; Liu, H. Improved hurricane track and intensity forecast using single field-of-view advanced IR sounding measurements. *Geophys. Res. Lett.* **2009**, *36*, 2009GL0382850. [CrossRef]
18. Wang, P.; Li, J.; Li, J.L.; Schmit, T.J.; Bai, W. Advanced infrared sounder subpixel cloud detection with imagers and its impact on radiance assimilation in NWP. *Geophys. Res. Lett.* **2014**, *41*, 1773–1780. [CrossRef]
19. Szyndel, M.D.E.; Kelly, G.; Thépaut, J.N. Evaluation of potential benefit of assimilation of SEVIRI water vapour radiance data from Meteosat-8 into global numerical weather prediction analyses. *Atmos. Sci. Lett.* **2005**, *6*, 105–111. [CrossRef]
20. Honda, T.; Kotsuki, S.; Lien, G.-Y.; Okamoto, K.; Miyoshi, T. Assimilation of Himawari-8 all-sky radiances every 10 min: Impact on precipitation and flood risk prediction. *J. Geophys. Res. Atmos.* **2018**, *123*, 965–976. [CrossRef]
21. Honda, T.; Miyoshi, T.; Lien, G.-Y.; Nishizawa, S.; Yoshida, R.; Adachi, S.A.; Terasaki, K.; Okamoto, K.; Tomita, H.; Bessho, K. Assimilating All-Sky Himawari-8 Satellite Infrared Radiances: A Case of Typhoon Soudelor (2015). *Mon. Weather Rev.* **2018**, *146*, 213–229. [CrossRef]
22. Goleberg, M.D.; Kilcoyne, H.; Cilkanek, H.; Mahta, A. Joint Polar Satellite System: The United States next generation civilian polar-orbiting environmental satellite system. *J. Geophys. Res. Atmos.* **2013**, *13*, 463–475.
23. Schmetz, J. Good Things Need Time: Progress with the First Hyperspectral Sounder in Geostationary Orbit. *Geophys. Res. Lett.* **2021**, *48*, e2021GL096207. [CrossRef]
24. Yang, J.; Zhang, Z.Q.; Wei, C.Y. Introducing the New Generation of Chinese Geostationary Weather Satellites, Fengyun-4. *Bull. Am. Meteorol. Soc.* **2017**, *98*, 1637–1658. [CrossRef]

25. Di, D.; Li, J.; Han, W.; Bai, W.G.; Wu, C.Q.; Menzel, W.P. Enhancing the Fast Radiative Transfer Model for FengYun-4 GIIRS by Using Local Training Profiles. *J. Geophys. Res. Atmos.* **2018**, *123*, 583–596. [CrossRef]
26. Yin, R.Y.; Han, W.; Gao, Z.Q.; Di, D. The evaluation of FY4A's Geostationary Interferometric Infrared Sounder (GIIRS) long-wave temperature sounding channels using the GRAPES global 4D-Var. *Q. J. R. Meteorol. Soc.* **2020**, *146*, 1459–1476. [CrossRef]
27. Cai, X.; Bao, Y.S.; Petropoulos, G.P.; Lu , F.; Lu, Q.F.; Zhu, L.H.; Wu, Y. Temperature and Humidity Profile Retrieval from FY4-GIIRS Hyperspectral Data Using Artificial Neural Networks. *Remote Sens.* **2016**, *12*, 1872. [CrossRef]
28. Ma, J.; Li, J.; Han, W.; Li, Z.L.; Zeng, Q.C.; Menzel, W.P.; Schmit, T.J.; Di, D.; Liu, C.-Y. Four-dimensional wind fields from geostationary hyperspectral infrared sounder radiance measurements with high temporal resolution. *Geophys. Res. Lett.* **2021**, *48*, e2021GL093794. [CrossRef]
29. Yao, S.H.; Li, G. Comparison of Three Convolution Neural Network Schemes to Retrieve Temperature and Humidity Profiles from the FY4A GIIRS Observations. *Remote Sens.* **2022**, *14*, 5112. [CrossRef]
30. Yin, R.Y.; Han, W.; Gao, Z.Q.; Li, J. Impact of high temporal resolution FY-4A Geostationary Interferometric Infrared Sounder (GIIRS) radiance measurements on Typhoon forecasts: Maria (2018) case with GRAPES global 4D-Var assimilation system. *Geophys. Res. Lett.* **2021**, *48*, e2021GL093672. [CrossRef]
31. Xie, Q.; Li, D.Q.; Yang, L.; Ma, Y.Y.; Pan, X.; Chen, M. Impact of assimilating atmospheric motion vectors from Himawari-8 and clear-sky radiance from FY-4A GIIRS on binary typhoons. *Atmos. Res.* **2023**, *144*, 106550. [CrossRef]
32. Zhang, L.; Niu, Z.Y.; Weng, F.Z.; Dong, P.M.; Huang, W.; Zhu, J. Impacts of direct assimilation of the FY-4A/GIIRS long-wave temperature Sounding Channel data on forecasting typhoon In-fa. *Remote Sens.* **2023**, *15*, 355. [CrossRef]
33. Nalli, N.R.; Gambacorta, A.; Liu, Q.H.; Barnet, C.D.; Tian, C.Y.; Iturbide-Sanchez, F.; Reale, T.; Sun, B.M.; Wilson, M.; Borg, L.; et al. Validation of Atmospheric Profile Retrievals From the SNPP NOAA-Unique Combined Atmospheric Processing System. Part 1: Temperature and Moisture. *IEEE Trans. Geosci. Remote. Sens.* **2018**, *56*, 180–190. [CrossRef]
34. Berndt, E.; Smith, N.; Burks, J.; White, K.; Esmaili, R.; Kuiciauskas, A.; Duran, E.; Allen, R.; LaFontaine, F.; Szkodzinski, J. Gridded Satellite Sounding Retrievals in Operational Weather Forecasting: Product Description and Emerging Applications. *Remote Sens.* **2020**, *12*, 3311. [CrossRef]
35. Erye, K. The WMO Vision for global observing systems in 2025: To what extent will it be met by space agencies' plans. In Proceedings of the ECMWF Annual Seminar, Reading, UK, 1–4 September 2014.
36. Li, J.; Huang, H.L. Retrieval of atmospheric profiles from satellite sounder measurements by use of the discrepancy principle. *Appl. Opt.* **1999**, *38*, 916–923. [CrossRef] [PubMed]
37. Li, J.; Wolf, W.W.; Menzel, W.P.; Zhang, W.J.; Huang, H.-L.; Achtor, T.H. Global Soundings of the Atmosphere from ATOVS Measurements: The Algorithm and Validation. *J. Appl. Meteor. Climatol.* **2000**, *39*, 1248–1268. [CrossRef]
38. He, M.; Wang, D.H.; Ding, W.Y.; Wan, Y.J.; Chen, Y.H.; Zhang, Y. A Validation of Fengyun4A Temperature and Humidity Profile Products by Radiosonde Observations. *Remote Sens.* **2019**, *11*, 2039. [CrossRef]
39. Du, M.B.; Cui, L.L.; Lu, F.; Peng, J.; Shi, J.; Liu, D.H.; Fan, H. Quality evaluation of FY-4A/GIIRS atmospheric temperature profile. *J. Infrared Millim.* **2023**, *42*, 399–409.
40. Gao, Y.; Mao, D.Y.; Wang, X.; Qin, D.Y. Evaluation of FY-4A Temperature Profile Products and Application to Winter Precipitation Type Diagnosis in Southern China. *Remote Sens.* **2022**, *14*, 2363. [CrossRef]
41. Feng, J.; Qin, X.H.; Wu, C.Q.; Zhang, P.; Yang, L.; Shen, X.S.; Han, W.; Liu, Y.Z. Improving typhoon predictions by assimilating the retrieval of atmospheric temperature profiles from the FengYun-4A's Geostationary Interferometric Infrared Sounder (GIIRS). *Atmos. Res.* **2022**, *208*, 106391. [CrossRef]
42. Wang, S.F.; Lu, F.; Feng, Y.T. An Investigation of the Fengyun-4A/B GIIRS Performance on Temperature and Humidity Retrievals. *Atmosphere* **2022**, *13*, 1830. [CrossRef]
43. Niu, Z.Y.; Zhang, L.; Han, Y.; Dong, P.M.; Huang, W. Performances between the FY-4A/GIIRS and FY-4B/GIIRS Long-Wave InfraRed (LWIR) channels under clear-sky and all-sky conditions. *Q. J. R. Meteorol. Soc.* **2023**, *146*, 1612–1628. [CrossRef]
44. Yang, W.Y.; Chen, Y.D.; Bai, W.G.; Sun, X.; Zheng, H.; Qin, L.Y. Evaluation of Temperature and Humidity Profiles Retrieved from Fengyun-4B and Implications for Typhoon Assimilation and Forecasting. *Remote Sens.* **2023**, *15*, 5339. [CrossRef]
45. Hurlbut, M.M.; Cohen, E.A. Environments of Northeast U.S. Severe Thunderstorm Events from 1999 to 2009. *Weather Forcasting* **2014**, *29*, 3–22. [CrossRef]
46. Haynes, K.; Stock, J.; Dostalek, J.; Anderson, C.; Ebert-Uphoff, I. Exploring the Use of Machine Learning to Improve Vertical Profiles of Temperature and Moisture. *Artif. Intell. Earth Syst.* **2023**, *3*, e220090. [CrossRef]
47. Bai ,W.G.; Zhang, P.; Liu, H.; Zhang, W.J.; Qi, C.L.; Ma, G.; Li, G.N. A Fast Piecewise-Defined Neural Network Method to Retrieve Temperature and Humidity Profile for the Vertical Atmospheric Sounding System of FengYun-3E Satellite. *IEEE Trans. Geosci. Remote. Sens.* **2023**, *61*, 1–10.
48. Di, D. Data Assimilation Research for Geosynchronous Interferometric Infrared Sounder Onboard FengYun-4 Satellite. Ph.D. Thesis, Chinese Academy of Meteorological Sciences, Beijing, China, 16 July 2019.
49. Liu, Z.Q.; Barker, D.M. Radiance Assimilation in WRF-Var: Implementation and Initial Results. Presented at the 7th WRF Users Workshop, Boulder, CO, USA, 19–22 June 2006. Available online: https://www.researchgate.net/publication/228868507 (accessed on 5 November 2024).
50. Buchhorn, M.; Smets, B.; Bertels, L.; Roo, B.D.; Lesiv, M.; Tsendbazar, N.-E.; Herold, M.; Fritz, S. Copernicus Global Land Service: Land Cover 100m: Collection 3: Epoch 2019: Globe. Available online: https://zenodo.org/records/3939050 (accessed on 5 November 2024).

51. Integration Dataset of Tibet Plateau Boundary. A Big Earth Data Platform for Three Poles. Available online: https://data.tpdc.ac.cn/en/data/61701a2b-31e5-41bf-b0a3-607c2a9bd3b3/ (accessed on 5 November 2024).
52. Zhou, Y.; Wang, X.Z.; Xu, C. Comprehensive evaluation of the precipitable water vapor products of Fengyun satellites via GNSS data over mainland China. *Atmos. Res.* **2024**, *300*, 107235. [CrossRef]
53. Bracken, I.; Martin, D. The generation of spatial population distributions from census centroid data. *Environ. Plan. A* **1989**, *21*, 537–543. [CrossRef]
54. Longley, P.A.; Goodchild, M.F.; Magurie, D.J.; Rhind, D.W. *Geographic Information Systems and Science*; Wiley: Chichester, NY, USA, 2001; p. 454.
55. Lu, G.Y.; Wong, D.W. An adaptive inverse-distance weighting spatial interpolation technique. *Comput. Geosci.* **2008**, *34*, 1044–1055. [CrossRef]
56. Operation Specification for Conventional High Altitude Meteorological Observation. Available online: https://www.cma.gov.cn/zfxxgk/gknr/flfgbz/bz/202203/t20220324_4624667.html#:~:text=%E5%B8%B8%E8%A7%84%E9%AB%98%E7%A9%BA%E6%B0%94%E8%B1%A1 (accessed on 5 November 2024).
57. Da, C. Preliminary assessment of the Advanced Himawari Imager (AHI) measurement onboard Himawari-8 geostationary satellite. *Remote Sens. Lett.* **2016**, *10*, 409–418. [CrossRef]
58. Ren, L. A case study of GOES-15 imager bias characterization with a numerical weather prediction model. *Front. Earth Sci.* **2024**, *300*, 107235. [CrossRef]
59. Huang, X.D.; Ma, Y.; Li, Y.X.; Yang, X.L. Spatiotemporal variation characteristics of snow cover over the Tibetan Plateau from 1980 to 2020. *J. Glaciol. Geocryol.* **2023**, *38*, 423–434.